Wang, Xuchen; Diaz-Rubio, Ana; Tretyakov, Sergei A.

Independent Control of Multiple Channels in Metasurface Devices

Published in:
Physical Review Applied

DOI:
10.1103/PhysRevApplied.14.024089

Published: 28/08/2020

Document Version
Publisher's PDF, also known as Version of record

Please cite the original version:
Wang, X., Diaz-Rubio, A., & Tretyakov, S. A. (2020). Independent Control of Multiple Channels in Metasurface Devices. *Physical Review Applied*, *14*(2), Article 024089. https://doi.org/10.1103/PhysRevApplied.14.024089

Independent Control of Multiple Channels in Metasurface Devices

Xuchen Wang,* Ana Díaz-Rubio, and Sergei A. Tretyakov
Department of Electronics and Nanoengineering, Aalto University, P.O. Box 15500, Aalto FI-00076, Finland

(Received 14 January 2020; revised 4 April 2020; accepted 16 July 2020; published 28 August 2020)

By analogy with electromagnetic networks that connect multiple input-output ports, metasurfaces can be considered as multiport devices capable of providing different functionalities for waves of different polarizations illuminating the surface from different directions. The main challenge in the design of such multichannel metasurfaces is to realize independent and full control of the electromagnetic response for each channel incidence, ensuring the fulfilment of the boundary condition at the metasurface. In this work, we demonstrate that by properly engineering the evanescent fields excited at each port (that is, for all possible illumination directions), it is possible to independently control the reflection or transmission for all different illuminations. Using the mode-matching method, we analyze the scattering properties of generic space-modulated impedance metasurfaces. This method, combined with mathematical optimization, allows us to find a surface-impedance profile that simultaneously ensures the desired electromagnetic responses at each port. We validate the technique via the design of phase-controlled multichannel retroreflectors and multichannel perfect absorbers. In addition, we demonstrate that the method is rather powerful in the design of other functional metasurfaces, such as multifunctional reflectors.

DOI: 10.1103/PhysRevApplied.14.024089

I. INTRODUCTION

Metasurfaces are ultrathin artificial material layers formed by subwavelength-sized meta-atoms, designed for specific manipulations of the amplitudes, phases, and polarization states of reflected and transmitted waves [1–8]. Conventional metasurfaces for the control of plane-wave reflection and transmission consist of uniform periodical arrangements of subwavelength meta-atoms. The period of these metasurfaces is below the diffraction limit, so that no higher-order propagating modes in free space exist. These metasurfaces obey the usual reflection law.

In the past decade, the concept of metasurfaces has been extended to periodical structures with period larger than half of the wavelength. In this case, multiple diffraction orders are allowed to exist in free space and the metasurface can scatter energy into many directions. The traditional design method for such devices is to control the local reflection and/or transmission phases according to the required phase distributions of the scattered fields. This method is based on the phased-array principle, also called the generalized laws of reflection and refraction [9]. This approach has been leveraged for the synthesis of ultrathin optical devices for anomalous reflection and refraction [9–11], lensing [12,13], holographic imaging [14,15], and so forth. However, those devices commonly suffer from reduced efficiencies due to impedance mismatch between the incident and diffracted waves [16–18].

Recent efforts on metasurface-based gratings have been focused on perfect energy transmission between two scattering channels. Representative works include perfect anomalous refraction realized with bianisotropic elements [18–22] and perfect anomalous reflection using the concepts of near-field engineering [23–26], meta-grating [27], and other alternative means [18,26]. Furthermore, it has been shown that the power carried by a wave incident from one direction can be redistributed between two channels [23,28,29] or among arbitrary numbers of diffraction modes [30–32].

However, in all of those works, the metasurfaces are designed only for one incident angle and the response for waves incident from other directions is actually not engineered. Thus, the surface does not provide any functionality for other illuminations. It is worth mentioning that some of these devices can naturally provide multiple functionalities for different incidences [28,33]; for example, an anomalous reflector can always serve as a retroreflector when illuminated from its isolated channel [33]. But those additional functionalities are unconsciously inherited from reciprocity and power conservation.

Recently, interest in multifunctional metasurfaces has increased significantly and new devices that perform different functionalities by switching the incident directions [28,33] or polarization states [34,35] have been proposed. For example, in Ref. [28], five-port retroreflectors have been experimentally demonstrated by engineering thespatial dispersion of a reactive surface. In Ref. [36], it has been demonstrated that the reflection phases for

*xuchen.wang@aalto.fi

incidence from two different angles can be independently controlled by exciting different resonant modes in meta-atoms. However, these approaches for independent control of channel responses are applicable only for specific functionalities and strongly rely on numerical optimizations that are time consuming—especially when the number of considered channels increases—and that do not provide versatile and systematic design tools for multichannel devices.

According to the Floquet theory, periodic planar structures scatter into infinite numbers of harmonics in free space, including far-field propagating modes and near-field evanescent modes. In the far zone, the propagating modes are equivalent to "open waveguides," supporting waves propagating along different directions in space that are analogous to "channels" in a multiport network [28,37]. Therefore, metasurfaces can be viewed as N-port networks, where the number of ports depends on the number of considered incidence and scattering directions. Here, in the spirit of the classical theory of multiport systems [38], we consider linear metasurfaces as multiport networks characterized by an $N \times N$ scattering matrix $\overline{\overline{S}}$, operating for plane waves propagating along N directions in space. We show that this scattering matrix can be engineered in an arbitrary way provided that the matrix does not violate reciprocity for reciprocal structures and energy conservation for lossless metasurfaces. As is well known from the theory of electromagnetic networks, for lossless and reciprocal metasurfaces, the scattering matrix is unitary and symmetric.

The design objective is to implement actual structures that realize a certain $\overline{\overline{S}}$ matrix. The challenge is to find homogenized surface parameters (such as surface impedances [1], polarizabilities [7], or susceptibilities [39]) for multichannel metasurfaces and synthesize meta-atom arrays that realize the desired functionalities without brute-force numerical optimizations [40]. Conventional approaches assume that the surface properties are determined by one set of incident, reflected, and transmitted waves, and the problem of finding parameters that can simultaneously satisfy the boundary condition by multiple sets of incident and scattered waves is not addressed. As we show in this paper, the key for solving this problem is to excite proper groups of evanescent modes for incidence from different directions. These engineered evanescent modes together with the desired propagating modes can satisfy one impedance boundary condition for multiple incidence and scattering scenarios. Thus, one metasurface can offer different functionalities for illumination from different directions.

Our work is based on rigorous analytical formulations for the calculations of scattering harmonics of an arbitrary periodical space-modulated metasurface. Using a simple mathematical optimization, one can synthesize a gradient sheet impedance that can provide the defined multiple functionalities. We show that the developed semianalytical method can be used in the design of various types of multichannel metasurfaces, controlling scattering directions, amplitudes, and phases for different manners of illumination.

II. DESIGN CONCEPT

In this work, we use the surface-impedance model as the homogenization model for multichannel metasurfaces. Surface impedance defines relations between surface-averaged tangential electric and magnetic fields on the metasurface. After the incident, reflected, and transmitted fields of metasurfaces are ascertained, the required surface impedance can be easily obtained via the current-field relations [[8], Sec. 2.4.3]. This method has been widely used in the synthesis of metasurfaces modeled by electric impedance sheets [41–43] and bianisotropic metasurfaces realized with cascaded impedance sheets [16,21,44,45]. For a given scattering matrix, the known theoretical methods can engineer only the scattering properties of metasurfaces according to one column of the scattering matrix and the properties defined in other columns cannot be intentionally engineered. In other words, once the required surface impedance for excitation of one port (for waves incident from a specific direction) is determined, the responses at other channels are fixed and not controllable.

One should note that the $\overline{\overline{S}}$ matrix of a metasurface describes only the reflection and transmission of propagating modes. Although evanescent modes are not explicitly present in the scattering matrix of multichannel metasurfaces, they actually offer additional degrees of freedom in the determination of the boundary condition, which can simultaneously provide the desired properties of the scattering matrix for propagating modes [18,23]. Based on this observation, we propose the following approach to the design of multichannel metasurfaces, For incidence from one port, we define the scattered propagating modes in the desired $\overline{\overline{S}}$ matrix as well as a set of evanescent harmonics with unknown complex amplitudes. Likewise, for incidence from other ports, we introduce other sets of evanescent harmonics. In principle, the invocation of an infinite number of evanescent modes provides complete freedom for finding a surface impedance that can realize the desired properties for incidences from all channels, that is, the creation of multiport metasurface devices with arbitrarily defined $\overline{\overline{S}}$ matrices.

The important question is how to determine the required evanescent modes for each incidence scenario. Analytically solving for the evanescent harmonics is not an easy or even possible task since large, up to infinite, numbers of evanescent modes should be considered in sets of nonlinear equations [25]. Solving one

specific design problem, Kwon [25] optimized complex amplitudes of evanescent modes using mathematical tools with the aim of finding a locally passive surface impedance for perfect anomalous reflection. However, the developed optimization algorithm is applicable only for lossless and impenetrable boundaries. This limitation does not allow optimization of the surface topology, since the effects of evanescent modes inside the metasurface volume are not considered in the impenetrable impedance model. For this reason, we introduce a more effective optimization method that can find the surface impedance for both lossy and lossless, as well as for both reflection- and transmission-type, multichannel metasurfaces.

Instead of optimizing a large number of evanescent modes, as is done in Ref. [25], we optimize the Fourier coefficients of the impedance profile until the optimized surface generates the desired propagating harmonics at multiple incidences. The optimized surface launches the proper set of auxiliary evanescent modes and there is no need to directly optimize them. The optimization method is introduced in Sec. III B.

III. THEORY FOR CALCULATION OF FLOQUET HARMONICS

In this section, using the mode-matching method [[46], Sec. 6.2], we develop a general theory for the calculation of the scattered harmonics of an arbitrary gradient impedance metasurface. Based on this theory, a mathematical optimization method is introduced to control the scattering properties of metasurfaces.

A. Harmonic analysis for an arbitrary periodic surface impedance

Figure 1(a) illustrates the scattering scenario, where a space-modulated impedance sheet $Z_s(z)$ is mounted on a dielectric substrate. The sheet impedance is periodically modulated (period D) with an arbitrary profile. Under plane-wave excitation, the gradient surface scatters into an infinite number of Floquet harmonics. The tangential wave vector of the Floquet modes can be written as $k_{zn} = k_0 \sin\theta_i + n\beta_M$, where $\beta_M = 2\pi/D$ is the spatial frequency of the surface impedance and n is the mode order [28]. Furthermore, θ_i is the incident angle and k_0 is the free-space wave number. Modes satisfying $|k_{zn}| < k_0$ propagate into the far zone at the angle θ_n, defined by

$$\sin\theta_n = -\frac{k_0 \sin\theta_i + n\beta_M}{k_0}. \tag{1}$$

If $|k_{zn}| > k_0$, the mode is evanescent, with a decaying amplitude along the surface normal. For a given surface impedance and incident wave, the amplitudes and phases of all the scattered harmonics can be uniquely determined using the mode-matching method [[46], Sec. 6.2], by enforcing the boundary condition on the surface. However, this process could be cumbersome if the structure consists of multiple layers (e.g., with a substrate or superstrate).

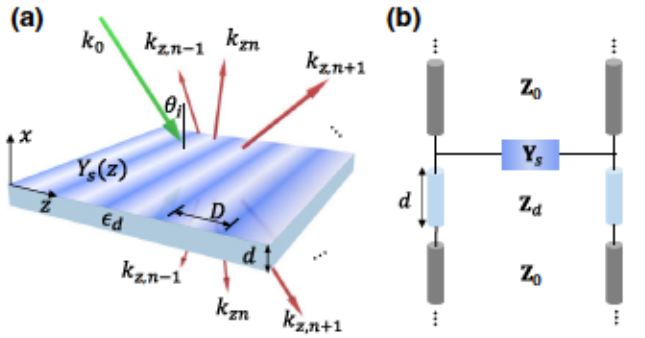

FIG. 1. (a) The scattering scenario of a space-modulated surface impedance based on a dielectric substrate. The wave is incident from $\theta = \theta_i$. (b) The equivalent circuit of the structure.

Here, we model the structure with a simple circuit model, shown in Fig. 1(b). Similarly to the conventional transmission-line model, the gradient surface impedance is represented by a shunt admittance and the substrate is modeled as a section of a shorted transmission line. The tangential electric and magnetic fields on the interfaces are analogized to the voltage and current, respectively. Considering that the metasurface scatters infinitely many Floquet modes, the equivalent voltage and current should also be composed of an infinite number of harmonics:

$$I_s(z) = \sum_{n=+\infty}^{-\infty} i_s^n e^{-\jmath k_{zn} z} \tag{2a}$$

and

$$V_s(z) = \sum_{n=+\infty}^{-\infty} v_s^n e^{-\jmath k_{zn} z}. \tag{2b}$$

The complex amplitudes of the voltage and current harmonics can be written in the form of vectors, $\vec{v}_s = [\ldots, v_s^{-1}, v_s^0, v_s^{+1}, \ldots]^T$ and $\vec{i}_s = [\ldots, i_s^{-1}, i_s^0, i_s^{+1}, \ldots]^T$. The quantity that relates the current and voltage vectors is called the admittance or impedance matrix, $\vec{i}_s = \mathbf{Y}_s \cdot \vec{v}_s$ or $\vec{v}_s = \mathbf{Z}_s \cdot \vec{i}_s$. Next, we aim to find the admittance and impedance matrices of gradient impedance surfaces.

Due to the spatial periodicity of the surface, the surface impedance $Z_s(z)$ or admittance $Y_s(z) = 1/Z_s(z)$ can be expanded into a Fourier series, as

$$Z_s(z) = \sum_{m=-\infty}^{+\infty} c_m e^{-\jmath m\beta_M z} \tag{3a}$$

or

$$Y_s(z) = \sum_{m=-\infty}^{+\infty} g_m e^{-jm\beta_M z}, \tag{3b}$$

where c_m and g_m are the Fourier coefficients of the impedance and admittance functions, respectively. Next, we use Eq. (3b) to derive the surface admittance matrix. Substituting Eqs. (2a), (2b), and (3b) into Ohm's law $I_s(z) = Y_s(z)V_s(z)$, we obtain

$$\sum_{n=-\infty}^{+\infty} i_s^n e^{-jk_{zn}z} = \sum_{n=-\infty}^{+\infty}\sum_{m=-\infty}^{+\infty} g_m v_s^n e^{-jk_{z,n+m}z}. \tag{4}$$

If n in the right-hand side of Eq. (4) is replaced with $n-m$, both sides have the same basis functions. In this case, the expression for the current of each harmonic can be simplified as

$$i_s^n = \sum_{m=-\infty}^{+\infty} g_m v_s^{n-m}. \tag{5}$$

It can be seen from Eq. (5) that the nth current component is coupled with all the voltage harmonics. Considering a finite number of modes (from $-N$ to $+N$), we can list $(2N+1)$ harmonics that will contribute in Eq. (5). This relation can be written in matrix form:

$$\begin{pmatrix} i_s^{-N} \\ i_s^{1-N} \\ \vdots \\ i_s^{+N} \end{pmatrix} = \begin{pmatrix} g_0 & g_{-1} & \cdots & g_{-2N} \\ g_1 & g_0 & \cdots & g_{1-2N} \\ \vdots & \vdots & \ddots & \vdots \\ g_{2N} & g_{2N-1} & \cdots & g_0 \end{pmatrix} \begin{pmatrix} v_s^{-N} \\ v_s^{1-N} \\ \vdots \\ v_s^{+N} \end{pmatrix}. \tag{6}$$

We can see that the current and voltage vectors are associated with a Toeplitz matrix $\mathbf{Y}_s$, which we call the *admittance matrix*. The admittance matrix is determined only by the Fourier coefficients of the modulation function, filling with $\mathbf{Y}_s(r,c) = g_{r-c}$ at the rth row and cth column. Alternatively, the surface can be characterized by the Toeplitz *impedance matrix* $\mathbf{Z}_s$, filling with Fourier terms of $Z_s(z)$, i.e. $\mathbf{Z}_s(r,c) = c_{r-c}$ [[47], Sec. 1]. Similarly to the scalar surface impedance [38], the transfer matrix (also known as *ABCD* matrix) corresponding to $\mathbf{Y}_s$ or $\mathbf{Z}_s$ reads

$$\mathbf{T}_s = \begin{bmatrix} \mathbf{I} & \mathbf{0} \\ \mathbf{Y}_s & \mathbf{I} \end{bmatrix} \quad \text{or} \quad \mathbf{T}_s = \begin{bmatrix} \mathbf{I} & \mathbf{0} \\ \mathbf{Z}_s^{-1} & \mathbf{I} \end{bmatrix}, \tag{7}$$

where $\mathbf{I}$ is the $(2N+1)\times(2N+1)$ identity matrix.

Next, we derive the transfer matrix of the dielectric slab $\mathbf{T}_d$. Since no modulation is assumed in dielectric layers, there are no coupling terms (off-diagonal terms) in the characteristic impedance matrix of dielectric $\mathbf{Z}_d$ and the matrix has only diagonal terms $\mathbf{Z}_d(n,n)$ (the rows and columns of the matrix are indexed from $-N$ to $+N$), where $\mathbf{Z}_d(n,n)$ is the characteristic impedance of the nth harmonic. The characteristic impedances for different polarization states are different and expressed as

$$\mathbf{Z}_d^{\mathrm{TE}}(n,n) = \frac{\mu_0\omega_0}{k_{xn}^d} \quad \text{and} \quad \mathbf{Z}_d^{\mathrm{TM}}(n,n) = \frac{k_{xn}^d}{\omega_0\epsilon_0\epsilon_d}, \tag{8}$$

where $k_{xn}^d = \sqrt{\omega_0^2\epsilon_0\epsilon_d\mu_0 - k_{zn}^2}$ is the normal component of the wave vector in the dielectric [[47], Sec. 2]. Due to the finite thickness of the substrates, their transfer matrices must include phase delay [38]. In this multimode system, we define propagation matrix $\mathbf{P}_d$, which also contains only diagonal terms $\mathbf{P}_d(n,n) = e^{-jk_{xn}^d d}$, modeling the phase delay of each harmonic in the dielectric slabs. The transfer matrix of the dielectric layers can be expressed as (see Sec. 3 of the Supplemental Material [47]; see also Ref. [48])

$$\mathbf{T}_d = \begin{bmatrix} (\mathbf{P}_d + \mathbf{P}_d^{-1})/2 & -\mathbf{Z}_d(\mathbf{P}_d - \mathbf{P}_d^{-1})/2 \\ -\mathbf{Z}_d^{-1}(\mathbf{P}_d - \mathbf{P}_d^{-1})/2 & (\mathbf{P}_d + \mathbf{P}_d^{-1})/2 \end{bmatrix}. \tag{9}$$

It is necessary to mention that the metasurface structure can contain a cascade of modulated impedance sheets (with the same periodicity D) separated by dielectric substrates. With knowledge of the transfer matrices of all constitutive layers, one can simply multiply them in sequence from the first illuminated layer,

$$\mathbf{T}_{\mathrm{tot}} = \cdots \mathbf{T}_s \mathbf{T}_d \cdots = \begin{bmatrix} \mathbf{A} & \mathbf{B} \\ \mathbf{C} & \mathbf{D} \end{bmatrix}, \tag{10}$$

where the dots represent additional constitutive layers for metasurfaces with multiple impedance sheets or dielectric layers. For impenetrable metasurfaces in which the transmission is blocked by a metallic plate, the total transfer matrix can be obtained by multiplying the transfer matrix of Eq. (10) by that of a metal plate [[47], Sec. 4].

The incident, reflected, and transmitted harmonics are written as vectors (denoted as $\vec{v}_{\mathrm{in}}$, $\vec{v}_{\mathrm{re}}$, and $\vec{v}_{\mathrm{tr}}$, respectively, for a TE-polarized wave) and are related by the total transfer matrix [[47], Sec. 5]

$$\begin{bmatrix} \vec{v}_{\mathrm{in}} + \vec{v}_{\mathrm{re}} \\ \mathbf{Y}_0 \cdot (\vec{v}_{\mathrm{in}} - \vec{v}_{\mathrm{re}}) \end{bmatrix} = \begin{bmatrix} \mathbf{A} & \mathbf{B} \\ \mathbf{C} & \mathbf{D} \end{bmatrix} \begin{bmatrix} \vec{v}_{\mathrm{tr}} \\ \mathbf{Y}_0 \cdot \vec{v}_{\mathrm{tr}} \end{bmatrix}, \tag{11}$$

where $\mathbf{Y}_0 = \mathbf{Z}_0^{-1}$ is the admittance matrix of free space [$\mathbf{Z}_0$ has the same format as $\mathbf{Z}_d$, only by replacing ϵ_d in Eq. (8) with 1]. We define reflection and transmission matrices that allow us to calculate reflected and transmitted harmonics for a given incident wave: $\vec{v}_{\mathrm{re}} = \mathbf{\Gamma} \cdot \vec{v}_{\mathrm{in}}$ and $\vec{v}_{\mathrm{tr}} = \mathbf{T} \cdot \vec{v}_{\mathrm{in}}$.

From Eq. (11), the transmission and reflection matrices are calculated as

$$\mathbf{T} = 2\left(\mathbf{A} + \mathbf{B}\mathbf{Y}_0 + \mathbf{Z}_0\mathbf{C} + \mathbf{Z}_0\mathbf{D}\mathbf{Y}_0\right)^{-1} \tag{12a}$$

and

$$\mathbf{\Gamma} = \left(\mathbf{A} + \mathbf{B}\mathbf{Y}_0\right)\mathbf{T} - \mathbf{I}. \tag{12b}$$

Note that Eqs. (12a) and (12b) are for a TE-polarized wave. For TM-polarized incidence [[47], Sec. 5], the reflection and transmission matrices are defined in terms of the current (the magnetic field), $\vec{i}_{\mathrm{re}} = \mathbf{\Gamma} \cdot \vec{i}_{\mathrm{in}}$ and $\vec{i}_{\mathrm{tr}} = \mathbf{T} \cdot \vec{i}_{\mathrm{in}}$, where

$$\mathbf{T} = 2\left(\mathbf{Y}_0\mathbf{A}\mathbf{Z}_0 + \mathbf{Y}_0\mathbf{B} + \mathbf{C}\mathbf{Z}_0 + \mathbf{D}\right)^{-1} \tag{13a}$$

and

$$\mathbf{\Gamma} = \left(\mathbf{C}\mathbf{Z}_0 + \mathbf{D}\right)\mathbf{T} - \mathbf{I}. \tag{13b}$$

We can see that $\mathbf{T}$ and $\mathbf{\Gamma}$ are derived for $(2N+1) \times (2N+1)$ square matrices. The columns and rows of $\mathbf{T}$ and $\mathbf{\Gamma}$ are indexed from $-N$ to $+N$. Likewise, the elements in $\vec{v}_{\mathrm{in}}$, $\vec{v}_{\mathrm{re}}$, and $\vec{v}_{\mathrm{tr}}$ (or $\vec{i}_{\mathrm{in}}$, $\vec{i}_{\mathrm{re}}$, and $\vec{i}_{\mathrm{tr}}$) are also indexed from $-N$ to $+N$. For illumination from one specific direction, the 0th element of the incidence vector is 1, while the rest of the positions are filled with zeros, e.g., $\vec{v}_{\mathrm{in}} = [\cdots, 0, 1, 0, \ldots]^T$. The multiplication results of the incidence vector with the reflection or transmission matrices is actually the 0th column of the corresponding reflection or transmission matrices. Therefore, for TE-polarized incidence, the nth order of reflected and transmitted harmonics can be found as $v_{\mathrm{re}}^n = \mathbf{\Gamma}(n, 0)$ and $v_{\mathrm{tr}}^n = \mathbf{T}(n, 0)$ (with the same for TM-polarized incidence), respectively, where $(n, 0)$ means the nth row and the 0th column.

B. Engineering scattering matrix by mathematical optimization

The presented analytical method is rigorous and general. For an incident plane wave with an arbitrary polarization state and incident angle, the scattered harmonics (including propagating and evanescent modes) are uniquely determined by the Fourier coefficients g_m (or c_m) that define the transfer matrix. On the other hand, if we expect the occurrence of some specific harmonics, e.g., propagating modes defined in the $\bar{\bar{S}}$ matrix of the multichannel metasurfaces, it is possible to find a proper set of g_m (or c_m) that ensures excitation of the desired harmonics.

However, the analytical relations between S_{ij} and g_m (or c_m) are not straightforward due to the need for complicated matrix operations. For this reason, in practice it is not possible to analytically solve g_m (or c_m) for desired harmonics.

Here, we use mathematical optimization tools available in the MATLAB package to find the optimal values of g_m (or c_m). Each element of the desired scattering matrix is an objective function in optimization. We denote the kth objective as O_k, which can be the amplitude or phase of one scattering parameter S_{ij}. In each trial of the optimization, MATLAB assumes an array of g_m (or c_m) and calculates the realized value F_k for each objective O_k, using the analytical formulas in Sec. III A. For a system with multiple objectives, we can define a cost function in the optimization code as

$$C = \sum_k \frac{|F_k - O_k|}{|O_k|}. \tag{14}$$

The cost function C is a sum of normalized errors calculated for all the objectives. Employing the *MultiStart* and *fmincon* optimization algorithms, MATLAB can search for the minimum value of C in the multidimensional parameter space. The optimization tools also allow us to set constraints on the Fourier coefficients in order to satisfy specific additional conditions, e.g., lossless, passive, capacitive, or inductive impedance. It is worth mentioning that, normally, the number of unknowns g_m (or c_m) should be larger than the numbers of objectives. The introduction of more Fourier terms increases the possibility of finding the optimal solution but, on the other hand, it may increase the optimization time. A similar optimization approach has been employed to determine the cascaded tensor admittances in the synthesis of bianisotropic metasurfaces [44].

In the following sections, we present the detailed process of optimization of the surface impedance for multichannel retroreflectors with independently and arbitrarily controlled reflection phases (Sec. IV), multichannel absorbers (Sec. V), and multifunctional reflectors (Sec. VI).

IV. PHASE-CONTROLLED MULTICHANNEL RETROREFLECTORS

A. Conventional retroreflectors

Let us first recall the design idea of a conventional three-channel retroreflector presented in [28]. A lossless impedance surface is positioned on a grounded substrate, as shown in Fig. 2. The period of the impedance-sheet modulation is set to $D = \lambda/2 \sin\theta_t$, where θ_t is the incident angle. The operating channels are defined at $\theta = +\theta_t, \theta = 0$, and $\theta = -\theta_t$, corresponding to Ports 1, 2, and 3, respectively.

The periodicity of the system allows only specular and retroreflection when the metasurface is illuminated by plane waves at $\theta = \pm\theta_t$. Since the period is subwavelength (for $30^\circ < \theta_t < 90^\circ$), waves incident from Port 2 are always fully reflected back to the specular direction

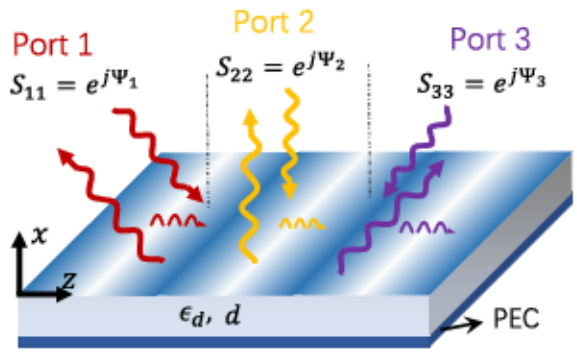

FIG. 2. The schematics for phase-controlled multichannel metasurfaces.

because waves to other channels are not allowed to propagate. In this case, if complete retroreflection is ensured for incidence from Port 1, full retroreflectance from Port 3 is automatically satisfied due to reciprocity. To design such metasurfaces, we only need to define the incident and reflected fields (both amplitudes and phases) for Port 1 and find the required surface impedance. Although the reflection phase of Port 1 can be arbitrarily defined, at other ports the reflection phases are not controllable.

Here, it is very necessary to clarify the definition of reflection phases of multichannel retroreflectors. The reflection phases depend on the chosen reference planes. For normal incidence (Port 2), it is clear that the reference plane is defined at the metasurface plane (the R_2 or R_2' plane in Fig. 3). But for oblique incidence (Port 1 or 3), it is necessary to first specify a reference point on the metasurface plane. The reference point (O or O' in Fig. 3) is the intersection point of the reference plane and the metasurface plane. Apparently, the reflection phase of a retroreflector depends on selection of the reference point. However, for metasurface retroreflectors, the sum of the reflection phases from Ports 1 and 3 is always a fixed value, no matter at which position the reference point is located. As shown in Fig. 3, when moving the reference point from

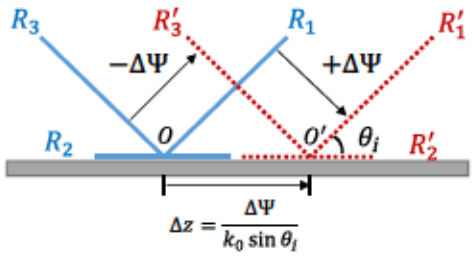

FIG. 3. The reference planes when moving the reference point from O to O'. R_1, R_2, and R_3 are the reference planes for Ports 1, 2, and 3, respectively, when the reference point is selected at O. R_1', R_2', and R_3' are the reference planes for Ports 1, 2, and 3 when the reference point is selected at O'.

O to O', the reference plane of Port 1 moves from R_1 to R_1' and the reflection phase increases by $\Delta\Psi$, but for Port 3, the reference plane moves from R_3 to R_3' and the phase decreases by the same value $\Delta\Psi$. Therefore, their sum is not dependent on the selection of the reference point. In other words, for a specific design, the reflection phases of Ports 1 and 3 can linearly decrease or increase in the opposite way when moving the reference point along the surface.

B. Multichannel control of reflection phase

The scattering matrix of a three-channel lossless retroreflector can be written as

$$\overline{\overline{S}} = \begin{bmatrix} e^{j\Psi_1} & 0 & 0 \\ 0 & e^{j\Psi_2} & 0 \\ 0 & 0 & e^{j\Psi_3} \end{bmatrix}. \tag{15}$$

Physically, the reflection phases from three ports can be arbitrary because the matrix is always symmetric and unitary. Therefore, it is possible to arbitrarily and independently engineer the reflection phases for incidence from each port.

The reflection matrix of metasurface $\mathbf{\Gamma}$ calculated from Eq. (12b) depends on the direction of incidence, i.e., we can define three different reflection matrices ($\mathbf{\Gamma}_1$, $\mathbf{\Gamma}_2$, and $\mathbf{\Gamma}_3$) for illumination from Ports 1, 2, and 3. Our goal is to realize retroreflection at each port with a specific set of reflection phases Ψ_1, Ψ_2, and Ψ_3. In this scenario, the cost function defined in Eq. (14) contains three objectives. First, we should ensure perfect retroreflection from Port 1 (order of $n = -1$), that is, ensure that the amplitude of the retroreflected wave is unity. This condition can be mathematically expressed as

$$F_1 = |\mathbf{\Gamma}_1(-1,0)|, \quad O_1 = |S_{11}| = 1. \tag{16}$$

As explained in Sec. IV A, perfect retroreflection at Port 1 automatically ensures the same functionality at Ports 2 and 3. The second objective is that the reflection phase from Port 2 (order $n = 0$) should be Ψ_2:

$$F_2 = \angle\mathbf{\Gamma}_2(0,0), \quad O_2 = \angle S_{22} = \Psi_2. \tag{17}$$

Finally, the last objective is that the sum of reflection phases from Ports 1 and 3 has a fixed value $\Psi_{13} = \Psi_1 + \Psi_3$:

$$F_3 = \angle\mathbf{\Gamma}_1(-1,0) + \angle\mathbf{\Gamma}_3(1,0), \tag{18a}$$

$$O_3 = \angle S_{11} + \angle S_{33} = \Psi_{13}. \tag{18b}$$

At this point, it is important to mention that optimization of the sum of Ψ_1 and Ψ_3 is more efficient than their individual

optimization, because the number of objectives is reduced. As we discuss in Sec. IV A, once the sum of the reflection phases is fixed, the desired reflection phases of Ports 1 and 3 can be realized by moving the reference point along the metasurface plane.

In this example, surface admittance [see Eq. (3b)] is used for modeling the gradient surface. It is easy to see that the functions F_k depend on the coefficients g_m. Consequently, optimization will allow us to search for solutions of g_m that can simultaneously satisfy equations $|F_k - O_k| = 0$ $(k = 1, 2, 3)$. In this particular example, there are three equations; therefore, we should introduce more than three coefficients g_m in the surface admittance expansion to find a solution. Moreover, in order to ensure that Y_s is a purely imaginary number (lossless metasurface), we need to take into consideration that g_m and g_{-m} are not independent and satisfy relations $\mathrm{Re}(g_m) + \mathrm{Re}(g_{-m}) = 0$ and $\mathrm{Im}(g_m) = \mathrm{Im}(g_{-m})$.

As an example, we realize a three-channel retroreflector with reflection phases $\Psi_1 = 0$, $\Psi_2 = -\pi/3$, and $\Psi_3 = \pi$. We introduce four complex unknowns g_0, $g_{\pm1}$, $g_{\pm2}$, and $g_{\pm3}$ and assume that the other Fourier coefficients are zero. The optimization results show that there may exist multiple solutions that minimize the cost function. For example, Fig. 4 shows two typical solutions. In Solution 1, the surface admittance in one unit cell exhibits both capacitive and inductive properties at different positions along the z axis, so this function crosses zero. This indicates that the required surface impedance contains some extreme values (zero admittance corresponds to infinite impedance), which may be difficult to implement by patterning a thin electric film. In this situation, we can impose additional constraints on g_m to ensure that the surface reactance is always capacitive or inductive along the metasurface, as shown in Solution 2. Figure 5 shows the calculated amplitudes and phases of the scattered harmonics for incidences from the three ports, for the two optimized admittance profiles. We can see that the two different solutions produce almost the same far fields for illumination from each port but the excited evanescent modes are totally different. The near fields affect the quality factor of the device (strong near fields mean a large quality factor and narrow bandwidth).

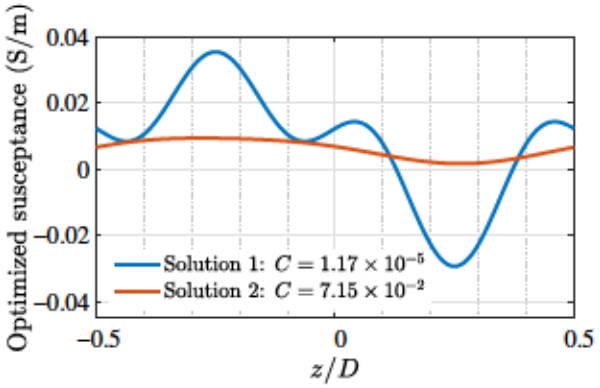

FIG. 4. The optimized grid susceptance profiles, $\mathrm{Im}[Y_s(z)]$, for the desired phase responses at three ports: $\Psi_1 = 0$, $\Psi_2 = -\pi/3$, and $\Psi_3 = \pi$. The optimized Fourier amplitudes for Solution 1 read $g_0 = j7.7 \times 10^{-3}$, $g_1 = 1.05 \times 10^{-2}$, $g_2 = j2.32 \times 10^{-3}$, and $g_3 = -5.73 \times 10^{-3}$. For Solution 2, $g_0 = j6.15 \times 10^{-3}$, $g_1 = (192.28 + j5.20) \times 10^{-5}$, $g_2 = (-1.023 + j3.007) \times 10^{-4}$, and $g_3 = 0$. The substrate is chosen as $d = 0.215$ mm and $\epsilon_d = 4.2$. The operating frequency is $f = 75$ GHz. The incidence is assumed to be TE polarized.

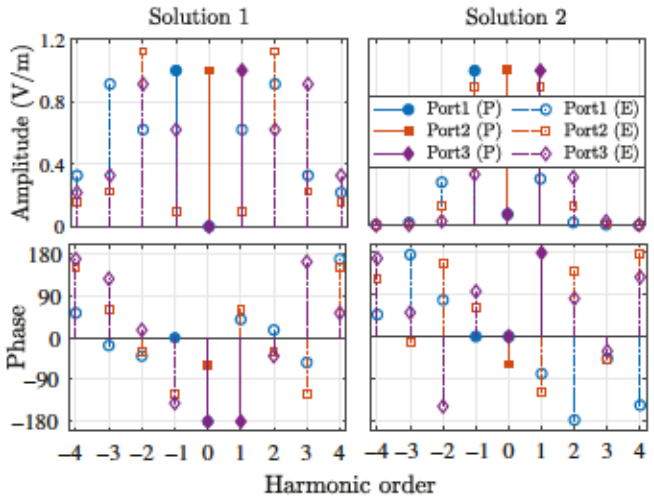

FIG. 5. The amplitudes and phases of the Fourier harmonics for the optimized solutions. "P" and "E" in the legend represent the propagating and evanescent modes. The amplitude of the incident electric field is 1 V/m.

The above example is only one specific assignment of reflection phases. The reflection phases at each port can be arbitrarily defined and the corresponding surface admittance can be efficiently optimized in MATLAB. We know that if we can find the surface impedance for arbitrary Ψ_2 and Ψ_{13}, the reflection phases at all three ports can be arbitrarily engineered. To check the potential of this approach, we carry out two parametric studies. In each study, we keep either Ψ_2 or Ψ_{13} constant and vary the other parameter within the values of $-\pi, -\pi/2, 0, +\pi/2$. Tables I and II present the optimized g_m. For each considered phase distribution, we can always find the required surface admittance with negligible errors.

C. Practical design

As soon as the spatially varying surface impedance or admittance is determined, we can locally implement the surface impedance according to the impedance-control method introduced in Ref. [40]. In the ideal case, if the implemented grid impedance changes continuously along

TABLE I. The optimized amplitudes of the Fourier harmonics for different values of the desired Ψ_2. In all cases, $\Psi_1 + \Psi_3 = \pi$.

Ψ_2	g_0	g_1	g_2	g_3	Optimization error
$-\pi$	$j1.88 \times 10^{-2}$	$j4.11 \times 10^{-5}$	$-j2.28 \times 10^{-4}$	$j7.72 \times 10^{-3}$	5.1×10^{-2}
$-\pi/2$	$j1.28 \times 10^{-2}$	$-j3.86 \times 10^{-3}$	$j7.37 \times 10^{-4}$	0	8.2×10^{-4}
0	$j7.31 \times 10^{-3}$	$j5.83 \times 10^{-3}$	$-j1.07 \times 10^{-3}$	$j5.89 \times 10^{-3}$	1.33×10^{-4}
$+\pi/2$	$-j9.28 \times 10^{-2}$	$j9.33 \times 10^{-2}$	$-j5.64 \times 10^{-2}$	$j2.59 \times 10^{-2}$	3.9×10^{-4}

the surface, the electromagnetic response of the metasurface should be the same as analytically predicted. However, in reality, due to limited fabrication fineness, each period of the surface should be split into a finite number of subcells. As we have demonstrated in Ref. [40], for the metasurfaces the functionalities of which rely on evanescent modes, the number of subinclusions in one unit should be sufficient to accurately excite the required evanescent modes, especially for the design with strong evanescent-field excitations.

Here, we aim to implement the design of multiport retroreflectors with phases at each channel $\Psi_1 = 0$, $\Psi_2 = -\pi/3$, and $\Psi_3 = \pi$. For simplicity, we choose the impedance profile of Solution 2 in Fig. 4, which corresponds to excitation of weaker evanescent modes than Solution 1. The unit cell is discretized into 20 subcells. Capacitive meta-atoms are synthesized as planar capacitors with the controlled gap width w_n. For large capacitance, we cannot shrink the gap further due to the resolution limitation of photolithography. Instead, we use meandering gaps of a cosine shape, as shown in Fig. 6. By varying the amplitudes of the cosine gap of each element a_n, we can realize and control the large sheet capacitance. After each element is engineered to ensure the required impedance value, we combine them and simulate the structure in Ansys HFSS without further structural optimization. Figures 7(a) and 7(b) show the simulated fields for the ideal impedance boundary and the implemented pattern, respectively. We can see in Fig. 7(b) that, for the actual topology, each port indeed reflects incident waves in the corresponding retrodirections. The reflection phases and field distributions are very close to the ideal scenario simulated with the perfect impedance boundary. For incidence from Port 1, the total field is at a maximum at the reference plane, meaning that $\Psi_1 = 0$. The total field at the reference plane of Port 3 is zero, which means that the reflection phase is $\Psi_3 = \pi$.

V. MULTICHANNEL PERFECT ABSORBERS

Following the generally accepted terminology [49,50], we define a planar surface as a "perfect absorber" if the theoretical absorptance equals unity (no reflection and no transmission) for plane-wave illumination at a certain (single) frequency, for a certain polarization, and at a certain incident angle. It is commonly believed that, in passive metasurfaces, such a perfect absorber can only be designed for one specific incident angle, with a few exceptions based on the use of spatial dispersion (see, e.g., Ref. [51]). Deviating from the defined angle, absorptance inevitably decreases due to impedance mismatch between the incident wave and the metasurface structure [52]. Full absorption for multiple illumination angles can be realized by employing some tunable materials in the absorbing structure, which can instantaneously adjust the input impedance of the metasurface with the change in the incident angle [53]. Although these devices can absorb energy from more than one direction, their operations rely on the modification of material properties and therefore they cannot work for simultaneous illuminations from multiple directions. Physical realizations of all-angle perfect absorbers (perfectly matched layers, PML) [54–56] require the use of active elements [56] or engineered strong spatial dispersion in bulk metamaterials [57].

A. Multichannel control of absorption

Here, we overcome this problem by using gradient metasurfaces with controlled channel responses. We utilize the same approach as presented above, introducing different sets of evanescent modes at different incident angles. These evanescent modes provide enough freedom to find the boundary condition, which ensures full absorption for multiple-incidence scenarios. We set the period of the metasurface below the diffraction limit, $D < \lambda/2$, so that there are no higher-order diffraction modes produced

TABLE II. The optimized amplitudes of the Fourier harmonics for different values of the desired $\Psi_1 + \Psi_3$. In all cases, $\Psi_2 = \pi$.

$\Psi_1 + \Psi_3$	g_0	g_1	g_2	g_3	Optimization error
$-\pi$	$j7.30 \times 10^{-3}$	$-j2.78 \times 10^{-3}$	$-j1.20 \times 10^{-2}$	0	0.021
$-\pi/2$	$j8.59 \times 10^{-3}$	$j4.77 \times 10^{-3}$	$-j9.40 \times 10^{-3}$	$-j3.22 \times 10^{-3}$	0.007
0	$j1.50 \times 10^{-2}$	$j1.36 \times 10^{-3}$	$j4.95 \times 10^{-3}$	$-j5.81 \times 10^{-3}$	0.045
$+\pi/2$	$j6.89 \times 10^{-3}$	$-j1.22 \times 10^{-3}$	$j2.15 \times 10^{-3}$	$-j5.60 \times 10^{-4}$	0.047

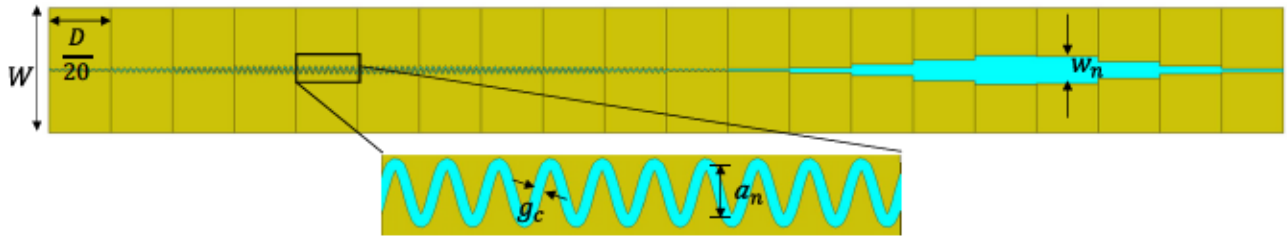

FIG. 6. The unit cell of the implemented device. The capacitive impedance of subcells 1–11 (from left to right) are controlled by meandering gaps varying with cosine functions. The gap width of the meandering slots is $g_c = 3$ μm. The amplitudes of the cosine functions for each subcell are different: $a_1 = 1.2$, $a_2 = 4.6$, $a_3 = 6.7$, $a_4 = 7.6$, $a_5 = 8.0$, $a_6 = 7.9$, $a_7 = 7.7$, $a_8 = 7.2$, $a_9 = 6.3$, $a_{10} = 4.8$, and $a_{11} = 2.1$, with units of micrometers. Elements 12–20 are synthesized by straight gaps with the gap width w_n for the nth subcell: w_n is set to $w_{12} = 5.0$, $w_{13} = 11.6$, $w_{14} = 25.6$, $w_{15} = 48$, $w_{16} = 67$, $w_{17} = 62$, $w_{18} = 38$, $w_{19} = 78$, and $w_{20} = 7.4$, with units of micrometers.

by the metasurface illuminated by plane waves from any direction. As illustrated in the left-hand part of Fig. 8(a), as the simplest example, we first target to realization of perfect absorption for two different incidence directions, $\theta = 0°$ (Port 2) and $\theta = +75°$ (Port 1), and perfect absorption at $\theta = -75°$ (Port 3) is unconsciously ensured due to reciprocity. The surface admittance is assumed to be a complex value varying as an even function of z, $Y_s(z) = Y_s(-z)$. Therefore, the Fourier coefficients of $Y_s(z)$ satisfy $g_m = g_{-m}$. Here, we use only two unknowns (g_0 and $g_{\pm 1}$) in the optimization. Note that the optimal sets of device parameters are not unique; the blue curves in Fig. 8(b) show one of the optimized solutions Z_{s1} ($Z_{s1} = 1/Y_{s1}$). The absorptance of the optimized surface as a function of the incident angle is calculated in Fig. 9 (blue curve). Due to the enforcement of perfect absorption at $\theta = 0°$ and $\theta = \pm 75°$, the absorptance in the angle spectrum remains high (above 80% between $\theta = -83°$ and $\theta = +83°$). However, there exist obvious absorption dips (close to $\theta = \pm 45°$) between the two defined angles of perfect absorption.

To avoid performance deterioration between the two perfect-absorption angles, one can impose more requirements on the metasurface performance, defining additional angles of perfect absorption. Here, we add one more objective in the optimization, enforcing perfect absorption at $\theta = \pm 45°$, as shown in the right-hand part of

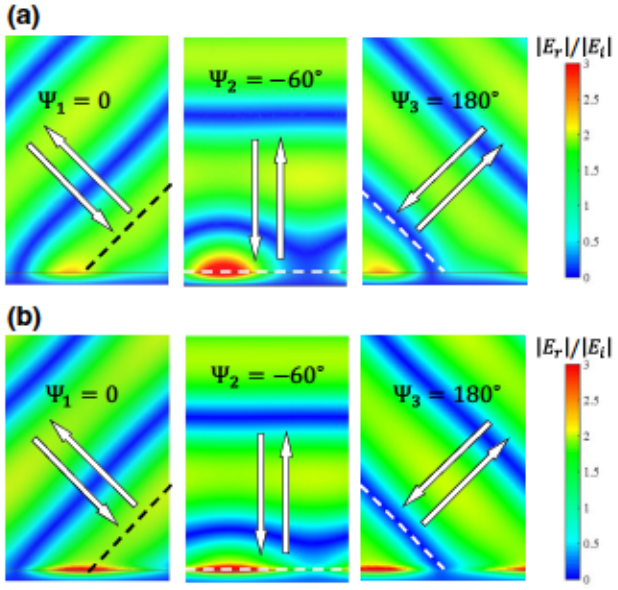

FIG. 7. The simulated total fields for incidence from three ports using (a) the impedance boundary condition and (b) the particular realizations shown in Fig. 6.

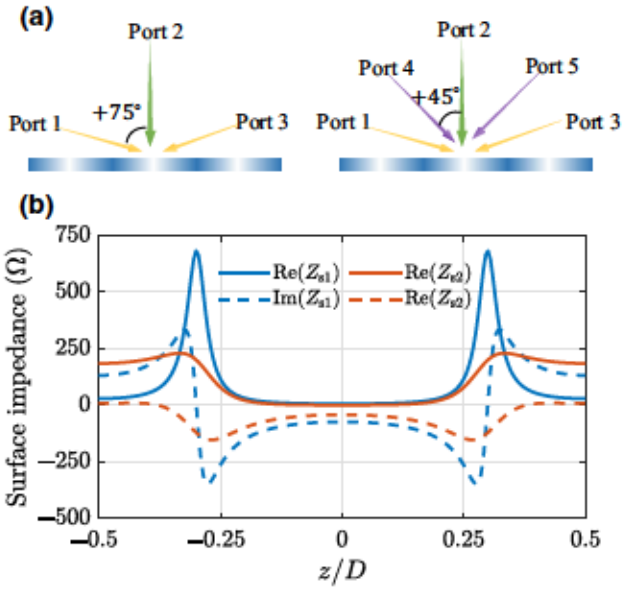

FIG. 8. (a) The schematics of three- (left) and five- (right) port multichannel absorbers. (b) The optimized surface impedance (in one period) for perfect absorption three- and five-port metasurface absorbers. The optimized parameters for $Z_{s1}(z)$ read $g_0 = (1.4 + 3.16j) \times 10^{-3}$, $g_1 = g_{-1} = (-1.083 + 51.92j) \times 10^{-4}$, $d = 500$ μm, $\epsilon_d = 4.2$, and $D = 0.419\lambda$. For $Z_{s2}(z)$, they read $g_0 = (2.894 + j8.543) \times 10^{-3}$, $g_1 = g_{-1} = (-1.251 + j6.017) \times 10^{-3}$, $g_2 = g_{-2} = j16.29 \times 10^{-4}$, $d = 743$ μm, $\epsilon_d = 11.7$, and $D = 0.457\lambda$. The operating frequency is $f = 75$ GHz. The incident wave is TM polarized.

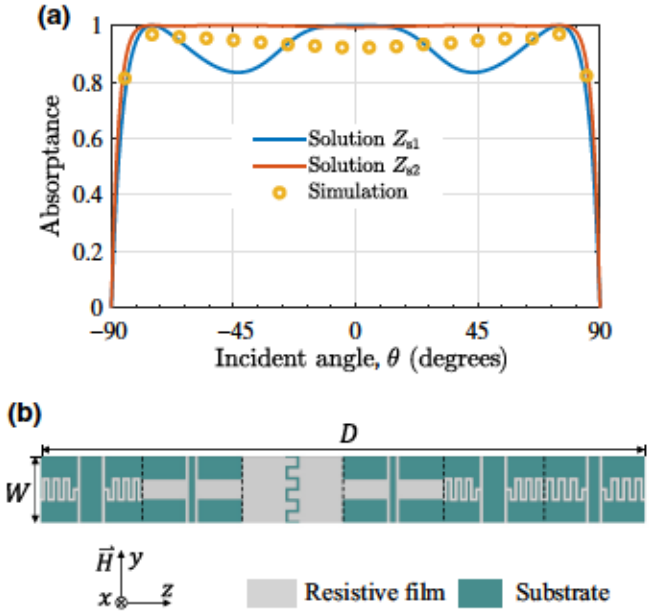

FIG. 9. The absorptance of the optimized impedance sheets in Fig. 8(b) as a function of the incident angle. The circles are simulated values of the implemented structure. (b) The implemented multichannel five-port absorber. Here, $D = 1829$ μm, $W = 200$ μm, and the other geometrical dimensions are specified in Ref. [[47], Sec. 6].

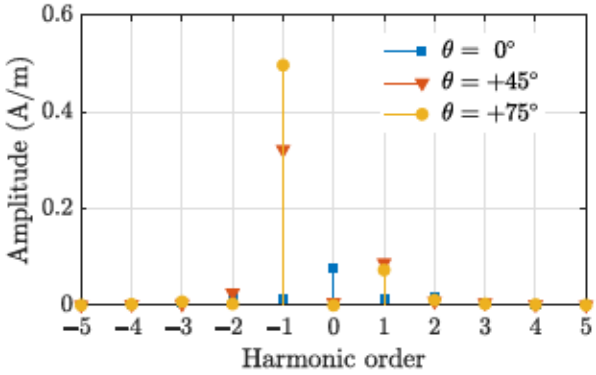

FIG. 10. The amplitudes of the scattered harmonics of five-port perfect absorbers (for Z_{s2}) for incidences from Ports 2 ($\theta = 0°$), 4 ($\theta = +45°$), and 1 ($\theta = +75°$). The amplitude of the incident magnetic field is 1 A/m.

Fig. 8(a) (five-port perfect absorber). The optimal surface impedance for a five-port perfect absorber is shown in Fig. 8(b) (red curves). One can see from Fig. 9 (red curve) that, after ensuring full absorption at $\theta = \pm 45°$, the device acts as a near-perfect absorber ($A > 99\%$) at all angles between $\theta = -80°$ and $\theta = +80°$. Figure 10 shows the excited Floquet harmonics of the five-port perfect absorber for incidence from different directions. As expected, different sets of evanescent modes are generated at the three incident angles.

From the physical point of view, this structure realizes multiple-angle perfect absorption by engineering spatial dispersion in the metasurface, resulting in wide-angle metasurface absorbers. In contrast to earlier studies [57] that considered bulk metamaterials, the desired performance is achieved by proper structuring of a single material sheet, allowing simple practical realizations.

B. Practical design

Sheets with the required spatially varying resistance and reactance can be realized either using distributed lumped components or by pattering an uniform material layer. A method for implementing complex surface impedance based on a uniform resistive layer has been introduced in [40,58]. The surface resistance can be controlled by the width or length of resistive strips and the surface reactance can be implemented by inductive lines or capacitive gaps. However, for some extreme values of the reactance, the required dimensions may be beyond the fabrication limitations. A typical example is the case of very high surface inductance, where long and very narrow metallic strips are required. For this reason, one may need to set additional constraints in the optimization process, restricting the optimization tools to search the results within practically achievable impedance ranges. The number of discretization points is also important for metasurface implementation. It is shown in Ref. [40] that the minimal number of discretization points depends on the strength of the excited evanescent fields. For stronger evanescent fields, more subelements are required in one unit cell, which may impose difficulties in fabrication. Since the solutions of these optimization problems are not unique, it is more favorable to select a solution that corresponds to weaker evanescent fields, as we do in Sec. IV C.

The optimized Z_{s2} in Fig. 8(b) takes into consideration the constraints of conventional fabrication techniques on the substrate thickness, its permittivity, and the maximum achievable reactance or resistance. In the optimization process, the dielectric permittivity is fixed at $\epsilon_d = 11.7$, corresponding to conventional silicon wafers. The grid impedance is implemented by patterning a 25-nm aluminum film with measured sheet resistivity 2 Ω/sq [40] and the dimensions are set with the limitations of the photolithography processes. The optimized maximum grid resistance and inductance cannot be too large; otherwise, we would need very narrow lines, the width of which would rival the fabrication limitations. Therefore, we set constraints on the grid resistance and inductance in the optimization as $\mathrm{Re}(Z_{s2}) < 250$ Ω and $\mathrm{Im}(Z_{s2}) < 10$ Ω. The peculiarities of the optimization codes are explained in Ref. [[47], Sec. 7]. We discretize the optimized impedance profile Z_{s2} into six elements and locally implement the required grid resistance and reactance. Then, we combine all the patterned cells [see Fig. 9(b)] and simulate the structure as a whole using HFSS. The

simulated performance exhibits high absorptance ($A > 92\%$) between $\theta = -80°$ and $\theta = +80°$. The discrepancy with the theoretical absorptance is caused mainly by the limited number of discretization elements. The performance can be further improved by using more subcells.

VI. MULTIFUNCTIONAL REFLECTORS

In principle, the scattering matrix of a multiport system can be arbitrarily defined if it does not violate fundamental physical laws. There are numerous practically important functionalities and in this section our target is to find the surface impedance realizing the multifunctional reflector envisioned in Ref. [28].

The device is a five-channel metasurface with periodicity $D = 2\lambda/\sin\theta_t$. As shown in Fig. 11(a), the metasurface can act as a perfect retroreflector when illuminated from $\theta = \pm\theta_t$, while under normal incidence, it splits the beam equally into the directions $\theta = \pm\arcsin(\sin\theta_t/2)$. In this case, we need to control the scattering properties from three ports: for incidence from Port 3, the wave splits equally between Ports 2 and 4, so that $|S_{43}| = |S_{23}| = 0.707$; for incidence from Ports 1 ($\theta = +\theta_t$) or 5 ($\theta = -\theta_t$), the waves bounce back to the corresponding retrodirections with $|S_{11}| = |S_{55}| = 1$. In this example, we choose to optimize the Fourier coefficients of the surface impedance defined in Eq. (3a). In the optimization, we introduce four unknowns c_m for the construction of the surface impedance

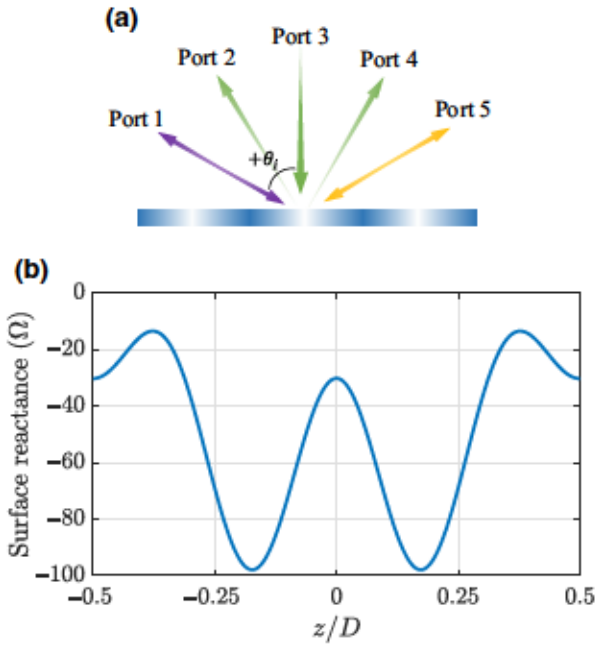

FIG. 11. (a) A schematic of the multifunctional reflector envisioned in Ref. [28]. (b) The optimized surface reactance in one period for $\theta_i = 60°$. The optimized substrate thickness is $d = 624\ \mu$m for the defined frequency at 75 GHz and a permittivity of $\epsilon_d = 13.9$. The incidence is assumed to be TE polarized.

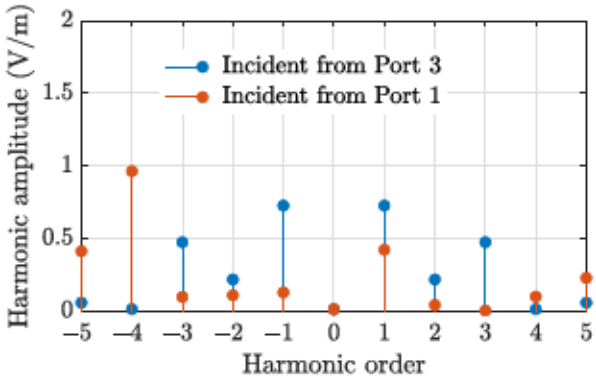

FIG. 12. The amplitudes of scattered harmonics for incidence from Port 1 ($\theta = +60°$) and Port 3 ($\theta = 0°$). The amplitude of incident electric field is 1 V/m.

and also set a constraint in the code to ensure a purely capacitive surface impedance (for simplicity of realization). In addition, the substrate permittivity and thickness are set as additional unknowns in order to increase the optimization freedom. The optimized surface impedance for $\theta_t = 60°$ is shown in Fig. 11(b). The scattered harmonics for incidences from Port 3 (beam-splitter operation) and Port 1 (which performs as a retroreflector) are calculated in Fig. 12. We can see that for normal incidence, the surface splits 95% of the impinging energy equally between Ports 2 ($n = -1$) and 4 ($n = +1$), while Ports 1 ($n = -2$) and 5 ($n = +2$) receive 5% of the energy in total. For incidence from Port 1 ($\theta = +60°$), almost all the energy (approximately 93%) is reflected back in the retrodirection, corresponding to the harmonic $n = -4$. Since we look for the surface impedance as an even function with respect to the z axis, the scattered harmonics for incidence from Port 5 are the same as for incidence from Port 1. The synthesis of the optimized capacitive surface impedance can follow the same method as we presented in Sec. IV C for the design of multichannel phase-controlled retroreflectors.

VII. CONCLUSIONS

In this paper, we introduce a general and efficient method for the independent control of port responses in multichannel multifunctional metasurfaces. To implement a desired scattering matrix of the metasurface, our idea is to find a set of evanescent modes excited at each incidence scenario, which together with the defined propagating modes simultaneously satisfy one impedance boundary condition. Instead of looking for a purely analytical solution of the problem, we use mathematical optimization tools to find the Fourier coefficients of the surface admittance expansion that realize the defined scattering matrix. Since the developed approach is general and systematic, it offers an attractive physics-based alternative for the inverse design of metasurfaces, which is based on massive simulations and machine learning [59,60].

From the physical point of view, the proposed method allows the engineering of strong spatial dispersion (the desired nonlocal response of the metasurface is defined by a set of evanescent modes carrying power along the metasurface), going beyond the known designs, which are limited to the engineering of the electric, magnetic, and bianisotropic properties of metasurfaces [7]. From the applications point of view, the presented examples demonstrate the possibility of creating multichannel metasurface devices for rather general control of reflection and transmission of waves between multiple specified directions in space. In particular, designs of phase-controlled multichannel retroreflectors, perfect absorbers for multiple incident angles and multifunctional reflectors are presented as examples. Note that the proposed multichannel functional reflectors are realized by structuring only one planar material sheet, without the need to engineer volumetric artificial materials.

ACKNOWLEDGMENTS

This work received funding from the European Union's Horizon 2020 research and innovation program Future Emerging Topics (FETOPEN) under Grant Agreement No. 736876. The work is also supported by the Aalto ELEC Doctoral school. We would like to thank Dr. Viktar Asadchy and Dr. Shuomin Zhong for helpful discussions.

[1] C. L. Holloway, E. F. Kuester, J. A. Gordon, J. O'Hara, J. Booth, and D. R. Smith, An overview of the theory and applications of metasurfaces: The two-dimensional equivalents of metamaterials, IEEE Antennas Propag. Mag. **54**, 10 (2012).

[2] A. V. Kildishev, A. Boltasseva, and V. M. Shalaev, Planar photonics with metasurfaces, Science **339**, 1232009 (2013).

[3] N. Yu and F. Capasso, Flat optics with designer metasurfaces, Nat. Mater. **13**, 139 (2014).

[4] S. B. Glybovski, S. A. Tretyakov, P. A. Belov, Y. S. Kivshar, and C. R. Simovski, Metasurfaces: From microwaves to visible, Phys. Rep. **634**, 1 (2016).

[5] S. A. Tretyakov, V. S. Asadchy, and A. Díaz-Rubio, in *World Scientific Handbook of Metamaterials and Plasmonics*, edited by E. Shamonina (World Scientific Publishing Co., Singapore, 2017) Vol. 4, Chap. 6, p. 249.

[6] A. Li, S. Singh, and D. Sievenpiper, Metasurfaces and their applications, Nanophotonics **7**, 989 (2018).

[7] V. Asadchy, A. Díiaz-Rubio, and S. Tretyakov, Bianisotropic metasurfaces: Physics and applications, Nanophotonics **7**, 1069 (2018).

[8] F. Yang and Y. Rahmat-Samii, eds., *Surface Electromagnetics: With Applications in Antenna, Microwave, and Optical Engineering* (Cambridge University Press, Cambridge, 2019).

[9] N. Yu, P. Genevet, M. A. Kats, F. Aieta, J.-P. Tetienne, F. Capasso, and Z. Gaburro, Light propagation with phase discontinuities: Generalized laws of reflection and refraction, Science **334**, 333 (2011).

[10] X. Ni, N. K. Emani, A. V. Kildishev, A. Boltasseva, and V. M. Shalaev, Broadband light bending with plasmonic nanoantennas, Science **335**, 427 (2012).

[11] S. Sun, K.-Y. Yang, C.-M. Wang, T.-K. Juan, W. T. Chen, C. Y. Liao, Q. He, S. Xiao, W.-T. Kung, G.-Y. Guo, *et al.*, High-efficiency broadband anomalous reflection by gradient meta-surfaces, Nano Lett. **12**, 6223 (2012).

[12] F. Aieta, P. Genevet, M. A. Kats, N. Yu, R. Blanchard, Z. Gaburro, and F. Capasso, Aberration-free ultrathin flat lenses and axicons at telecom wavelengths based on plasmonic metasurfaces, Nano Lett. **12**, 4932 (2012).

[13] X. Chen, L. Huang, H. Mühlenbernd, G. Li, B. Bai, Q. Tan, G. Jin, C.-W. Qiu, S. Zhang, and T. Zentgraf, Dual-polarity plasmonic metalens for visible light, Nat. Commun. **3**, 1 (2012).

[14] X. Ni, A. V. Kildishev, and V. M. Shalaev, Metasurface holograms for visible light, Nat. Commun. **4**, 1 (2013).

[15] Y. Yifat, M. Eitan, Z. Iluz, Y. Hanein, A. Boag, and J. Scheuer, Highly efficient and broadband wide-angle holography using patch-dipole nanoantenna reflectarrays, Nano Lett. **14**, 2485 (2014).

[16] J. P. Wong, A. Epstein, and G. V. Eleftheriades, Reflectionless wide-angle refracting metasurfaces, IEEE Antennas Wirel. Propag. Lett. **15**, 1293 (2015).

[17] N. M. Estakhri and A. Alù, Wave-Front Transformation with Gradient Metasurfaces, Phys. Rev. X **6**, 041008 (2016).

[18] V. S. Asadchy, M. Albooyeh, S. N. Tcvetkova, A. Díaz-Rubio, Y. Ra'di, and S. Tretyakov, Perfect control of reflection and refraction using spatially dispersive metasurfaces, Phys. Rev. B **94**, 075142 (2016).

[19] A. Epstein and O. Rabinovich, in *12th European Conference on Antennas and Propagation (EuCAP 2018)* (London, 2018), p. 1.

[20] G. Lavigne, K. Achouri, V. S. Asadchy, S. A. Tretyakov, and C. Caloz, Susceptibility derivation and experimental demonstration of refracting metasurfaces without spurious diffraction, IEEE Trans. Antennas Propag. **66**, 1321 (2018).

[21] M. Chen, E. Abdo-Sánchez, A. Epstein, and G. V. Eleftheriades, Theory, design, and experimental verification of a reflectionless bianisotropic Huygens' metasurface for wide-angle refraction, Phys. Rev. B **97**, 125433 (2018).

[22] H. Kazemi, M. Albooyeh, and F. Capolino, Simultaneous Perfect Bending and Polarization Rotation of Electromagnetic Wavefront Using Chiral Gradient Metasurfaces, Phys. Rev. Appl. **13**, 024078 (2020).

[23] A. Epstein and G. V. Eleftheriades, Synthesis of Passive Lossless Metasurfaces Using Auxiliary Fields for Reflectionless Beam Splitting and Perfect Reflection, Phys. Rev. Lett. **117**, 256103 (2016).

[24] A. Díaz-Rubio, V. S. Asadchy, A. Elsakka, and S. A. Tretyakov, From the generalized reflection law to the realization of perfect anomalous reflectors, Sci. Adv. **3**, e1602714 (2017).

[25] D.-H. Kwon, Lossless scalar metasurfaces for anomalous reflection based on efficient surface field optimization, IEEE Antennas Wirel. Propag. Lett. **17**, 1149 (2018).

[26] A. M. Wong and G. V. Eleftheriades, Perfect Anomalous Reflection with a Bipartite Huygens' Metasurface, Phys. Rev. X **8**, 011036 (2018).

[27] Y. Ra'di, D. L. Sounas, and A. Alù, Metagratings: Beyond the Limits of Graded Metasurfaces for Wave Front Control, Phys. Rev. Lett. **119**, 067404 (2017).

[28] V. Asadchy, A. Díaz-Rubio, S. Tcvetkova, D.-H. Kwon, A. Elsakka, M. Albooyeh, and S. Tretyakov, Flat Engineered Multichannel Reflectors, Phys. Rev. X **7**, 031046 (2017).

[29] A. Epstein and O. Rabinovich, Unveiling the Properties of Metagratings via a Detailed Analytical Model for Synthesis and Analysis, Phys. Rev. Appl. **8**, 054037 (2017).

[30] V. Popov, F. Boust, and S. N. Burokur, Controlling Diffraction Patterns with Metagratings, Phys. Rev. Appl. **10**, 011002 (2018).

[31] V. Popov, F. Boust, and S. N. Burokur, Beamforming with metagratings at microwave frequencies: Design procedure and experimental demonstration, IEEE Trans. Antennas Propag. **68**, 1533 (2019).

[32] O. Rabinovich and A. Epstein, Arbitrary diffraction engineering with multilayered multielement metagratings, IEEE Trans. Antennas Propag. **68**, 1553 (2019).

[33] L.-Z. Yin, T.-J. Huang, F.-Y. Han, J.-Y. Liu, and P.-K. Liu, Terahertz multichannel metasurfaces with sparse unit cells, Opt. Lett. **44**, 1556 (2019).

[34] C. Zhang, F. Yue, D. Wen, M. Chen, Z. Zhang, W. Wang, and X. Chen, Multichannel metasurface for simultaneous control of holograms and twisted light beams, ACS Photonics **4**, 1906 (2017).

[35] C. Zhang, F. Dong, Y. Intaravanne, X. Zang, L. Xu, Z. Song, G. Zheng, W. Wang, W. Chu, and X. Chen, Multichannel Metasurfaces for Anticounterfeiting, Phys. Rev. Appl. **12**, 034028 (2019).

[36] S. M. Kamali, E. Arbabi, A. Arbabi, Y. Horie, M. Faraji-Dana, and A. Faraon, Angle-Multiplexed Metasurfaces: Encoding Independent Wavefronts in a Single Metasurface under Different Illumination Angles, Phys. Rev. X **7**, 041056 (2017).

[37] M. Guglielmi and A. A. Oliner, Multimode network description of a planar periodic metal-strip grating at a dielectric interface. I. Rigorous network formulations, IEEE Trans. Microw. Theory Tech. **37**, 534 (1989).

[38] D. M. Pozar, *Microwave Engineering* (John Wiley & Sons, Hoboken, New Jersey, 2009).

[39] K. Achouri, M. A. Salem, and C. Caloz, General metasurface synthesis based on susceptibility tensors, IEEE Trans. Antennas Propag. **63**, 2977 (2015).

[40] X. Wang, A. Díaz-Rubio, V. S. Asadchy, G. Ptitcyn, A. A. Generalov, J. Ala-Laurinaho, and S. A. Tretyakov, Extreme Asymmetry in Metasurfaces via Evanescent Fields Engineering: Angular-Asymmetric Absorption, Phys. Rev. Lett. **121**, 256802 (2018).

[41] F. Elek, B. B. Tierney, and A. Grbic, Synthesis of tensor impedance surfaces to control phase and power flow of guided waves, IEEE Trans. Antennas Propag. **63**, 3956 (2015).

[42] G. Minatti, M. Faenzi, E. Martini, F. Caminita, P. De Vita, D. González-Ovejero, M. Sabbadini, and S. Maci, Modulated metasurface antennas for space: Synthesis, analysis and realizations, IEEE Trans. Antennas Propag. **63**, 1288 (2014).

[43] B. H. Fong, J. S. Colburn, J. J. Ottusch, J. L. Visher, and D. F. Sievenpiper, Scalar and tensor holographic artificial impedance surfaces, IEEE Trans. Antennas Propag. **58**, 3212 (2010).

[44] C. Pfeiffer and A. Grbic, Bianisotropic Metasurfaces for Optimal Polarization Control: Analysis and Synthesis, Phys. Rev. Appl. **2**, 044011 (2014).

[45] A. Epstein and G. V. Eleftheriades, Arbitrary power-conserving field transformations with passive lossless omega-type bianisotropic metasurfaces, IEEE Trans. Antennas Propag. **64**, 3880 (2016).

[46] R.-B. Hwang, *Periodic Structures: Mode-Matching Approach and Applications in Electromagnetic Engineering* (John Wiley & Sons, Singapore, 2012), Chap. 6.2, p. 264.

[47] See the Supplemental Material at http://link.aps.org/supplemental/10.1103/PhysRevApplied.14.024089 for additional information.

[48] Y. Hadad, J. C. Soric, and A. Alù, Breaking temporal symmetries for emission and absorption, Proc. Natl. Acad. Sci. **113**, 3471 (2016).

[49] N. I. Landy, S. Sajuyigbe, J. J. Mock, D. R. Smith, and W. J. Padilla, Perfect Metamaterial Absorber, Phys. Rev. Lett. **100**, 207402 (2008).

[50] R. Alaee, M. Albooyeh, and C. Rockstuhl, Theory of metasurface based perfect absorbers, J. Phys. D: Appl. Phys. **50**, 503002 (2017).

[51] D. Zhirihin, C. Simovski, P. Belov, and S. Glybovski, Mushroom high-impedance metasurfaces for perfect absorption at two angles of incidence, IEEE Antennas Wirel. Propag. Lett. **16**, 2626 (2017).

[52] M. Diem, T. Koschny, and C. M. Soukoulis, Wide-angle perfect absorber/thermal emitter in the terahertz regime, Phys. Rev. B **79**, 033101 (2009).

[53] X. Wang and S. A. Tretyakov, in *2018 12th International Congress on Artificial Materials for Novel Wave Phenomena (Metamaterials)* (IEEE, Espoo, Finland, 1803), p. 430.

[54] R. W. Ziolkowski, The design of Maxwellian absorbers for numerical boundary conditions and for practical applications using engineered artificial materials, IEEE Trans. Antennas Propag. **45**, 656 (1997).

[55] R. W. Ziolkowski, Maxwellian material based absorbing boundary conditions, Comput. Methods Appl. Mech. Eng. **169**, 237 (1999).

[56] S. Tretyakov and T. Kharina, The perfectly matched layer as a synthetic material with active inclusions, Electromagnetics **20**, 155 (2000).

[57] S. Tretyakov, Uniaxial omega medium as a physically realizable alternative for the perfectly matched layer (PML), J. Electromagnetic Waves Appl. **12**, 821 (1998).

[58] X. Wang, A. Díaz-Rubio, A. Sneck, A. Alastalo, T. Mäkelä, J. Ala-Laurinaho, J.-F. Zheng, A. V. Räisänen, and S. A. Tretyakov, Systematic design of printable metasurfaces: Validation through reverse-offset printed millimeter-wave absorbers, IEEE Trans. Antennas Propag. **66**, 1340 (2018).

[59] Z. Liu, D. Zhu, S. P. Rodrigues, K.-T. Lee, and W. Cai, Generative model for the inverse design of metasurfaces, Nano Lett. **18**, 6570 (2018).

[60] E. S. Harper, E. J. Coyle, J. P. Vernon, and M. S. Mills, Inverse design of broadband highly reflective metasurfaces using neural networks, Phys. Rev. B **101**, 195104 (2020).